High capacity anode materials for Li-Ion Batteries Based on Spinel Metal Oxides AMn2O4 (A= Co, Ni, and Zn)

Courtel, Fabrice M.; Duncan, Hugues; Abu-Lebdeh, Yaser; Davidson, Isobel J.

Publisher's version / la version de l'éditeur:
Journal of Materials Chemistry, 21, 2011, pp. 10206-10218, 2011-05-26

Web page / page Web
http://dx.doi.org/10.1039/C0JM04465B
http://nparc.cisti-icist.nrc-cnrc.gc.ca/npsi/ctrl?action=rtdoc&an=18194625&lang=en
http://nparc.cisti-icist.nrc-cnrc.gc.ca/npsi/ctrl?action=rtdoc&an=18194625&lang=fr

Journal of Materials Chemistry

Cite this: DOI: 10.1039/c0jm04465b

www.rsc.org/materials

PAPER

High capacity anode materials for Li-ion batteries based on spinel metal oxides AMn_2O_4 (A = Co, Ni, and Zn)†

Fabrice M. Courtel,‡ Hugues Duncan,‡ Yaser Abu-Lebdeh* and Isobel J. Davidson

Received 20th December 2010, Accepted 15th February 2011
DOI: 10.1039/c0jm04465b

Manganites of transition and/or post-transition metals, AMn_2O_4 (where A was Co, Ni or Zn), were synthesized by a simple and easily scalable co-precipitation route and were evaluated as anode materials for Li-ion batteries. The obtained powders were characterized by SEM, TEM, and XRD techniques. Battery cycling showed that $ZnMn_2O_4$ exhibited the best performance (discharge capacity, cycling, and rate capability) compared to the two other manganites and their corresponding simple oxides. Further studies on the effect of different sintering temperatures (from 400 to 1000 °C) on particle size were performed, and it is found that the size of the particles had a significant effect on the performance of the batteries. The optimum particle size for $ZnMn_2O_4$ is found to be 75–150 nm. In addition, the use of water-soluble and environmentally friendly binders, such as lithium and sodium salts of carboxymethylcellulose, greatly improved the performance of the batteries compared to the conventional binder, PVDF. Finally, $ZnMn_2O_4$ powder sintered at 800 °C (<150 nm) and the use of the in-house synthesized lithium salt of carboxymethylcellulose (LiCMC) binder gave the best battery performance: a capacity of 690 mA h g^{-1} (3450 mA h mL^{-1}) at C/10, along with good rate capability and excellent capacity retention (88%).

Introduction

Li-ion batteries are the state-of-the-art in battery technology due to their ability to deliver high energy and long cycle life, and therefore they are successfully used in consumer electronic products and strongly considered for a wide variety of mobile (*e.g.* electric vehicle) and stationary (*e.g.* smart grid) applications. Most commercial batteries use graphitic carbon as the anode material[1] due to its low cost, long cycle life, and very stable capacity. However, the reversible electrochemical intercalation of lithium ions in its structure leads to a first-stage graphite intercalation compound with a composition of one lithium for six carbons, "LiC_6", which results in capacities limited to only 372 mA h g^{-1} and 830 mA h mL^{-1}. Alternative anode materials are hence currently being investigated with the focus on those based on mechanisms other than intercalation. One of the most common mechanisms is metals or metalloids that can electrochemically and reversibly alloy with lithium, such as tin ($SnLi_{4.4}$, 993 mA h g^{-1}), silicon ($SiLi_{4.4}$, 4200 mA h g^{-1}), antimony ($SbLi_3$, 660 mA h g^{-1}), and aluminium (LiAl, 994 mA h g^{-1}).[1–6] Tin and silicon are the most attractive as they provide much higher gravimetric capacities, 3 to 10 times greater than graphite, and are also denser than carbon, thus providing very high volumetric capacities, 7300 mA h mL^{-1} and 8320 mA h mL^{-1}, respectively. However, tin and silicon anodes suffer from large structural volume changes during charge/discharge cycling of the battery reaching 300–400% for silicon[1,7,8] and 260% for tin,[1] which gives rise to mechanical stresses that lead to cracks, eventual disintegration of the electrode and a failure of the battery.[9] Still, certain strategies can be used to overcome the problem, such as altering the composition of the alloy with foreign atom(s) at low and high concentrations, or structuring the alloy into morphologies that lead to better accommodation of volume changes, or the use of organic binders other than the conventional polyvinylidene fluoride (PVDF).[10]

Except for TiO_2, in its metastable brookite structure, most metal oxides (MOs) cannot intercalate lithium ions (0.76 Å) into their lattice structure due to the lack of free interstices with the right geometry (octahedral and preferably tetrahedral) and size.[11] They rather undergo an electrochemical reaction where the metal cation is reduced and embedded into an inactive Li_2O matrix and subsequently alloys with lithium such as in the case of SnO_2 (777 mA h g^{-1}) and Sb_2O_3 (552 mA h g^{-1}). For other MOs, where M is a transition metal (TM) such as Cr, Mn, Fe, Co, Ni, and Cu,

National Research Council Canada, 1200 Montreal Road, Ottawa, Ontario, K1A 0R6, Canada. E-mail: Yaser.Abu-Lebdeh@nrc-cnrc.gc.ca; Fax: +1 613 991-2384; Tel: +1 613 949-4184

† Electronic supplementary information (ESI) available: XRD of the commercial CoO powder and the NiO powder sintered at 400 °C; CVs of half-cells made using commercial CoO and NiO sintered at 400 °C; CVs of half-cells made using $CoMn_2O_4$ sintered at 800 °C and $NiMn_2O_4$ sintered at 400 °C; SEM, TEM and battery performance of $ZnMn_2O_4$ sintered for 16 h at 800 °C; the conversion reaction equations of $CoMn_2O_4$ and $NiMn_2O_4$ (PDF). See DOI: 10.1039/c0jm04465b

‡ Fabrice M. Courtel and Hugues Duncan contributed equally to this work.

the formation of an alloy with lithium is not possible; therefore, they interact with lithium in a third mechanism giving capacities experimentally ranging from 700 to 900 mA h g^{-1},[1,12] which translates to volumetric capacities ranging from 3500 to 4500 mA h mL^{-1} (assuming an average density of ~5 g mL^{-1}).[13] These simple transition metal oxides (TMOs) are poor electronic conductors with band gaps ranging from 3 to 4 eV[14] and also have no suitable free sites for the insertion of lithium ions; for instance CoO and NiO have an interstice-free rock-salt structure. Poizot *et al.* have shown that these TMOs undergo a reversible conversion reaction where the TMO is reduced into TM nanoparticles (1–2 nm) embedded into a matrix of Li_2O upon discharge [*e.g.* $NiO + 2Li^+ + 2e^- \leftrightarrow Ni + Li_2O$].[12] The formation of TM nanoparticles during the first discharge reaction overcomes the insulating nature of the TMOs. However, unlike in the case of the MOs (*e.g.* SnO_2 and Sb_2O_3), the Li_2O matrix that is formed during the first discharge is in this case completely active (*i.e.* decomposable), and the TM nanoparticles are oxidizable back into TMO nanoparticles. As explained by Poizot *et al.*, it is believed that the size confinement of the TM nanoparticles enhances their electrochemical activity towards the decomposition of the Li_2O matrix[12]—a phenomenon similar to LiF in metal fluorides as explained by Maier in terms of a nanoeffect resulting from increased surface energies of confined space.[15] This oxidation reaction does not occur at a microscopic scale; particles of TMs must be nanometric and in close contact with Li_2O for this solid-state oxidation reaction to occur.[1] Like the TMOs, ZnO has an interstice-free würtzite structure that does not allow any lithium insertion, but as a post-transition metal oxide, ZnO behaves differently. It first goes through the same conversion reaction as observed for TMOs; however, it further reacts with lithium by forming a ZnLi alloy.[16,17]

Manganese oxide,[18,19] iron oxide,[20–22] cobalt oxide,[12] nickel oxide,[12,23] copper oxide[12,24] and zinc oxide[25] have been widely investigated. All these MOs exhibit a large difference between the reduction and the oxidation potentials which can easily be calculated from thermodynamic data as demonstrated by Li *et al.*[26] In addition, during experimental cycling a large overpotential is observed for both reactions due to slow kinetics associated with solid-state reactions; thus a large potential window is required in order to obtain an optimum capacity. Due to these kinetic limitations, only those that show an electromotive force (EMF) above 1 V *vs.* Li/Li^+ will be reduced before the electrodeposition of lithium metal.[26] However, in order to limit the oxidation potential and keep a convenient battery output voltage (*i.e.* over 2 V), the EMF should not be above 1.6–1.7 V *vs.* Li/Li^+. This limits the number of materials that can be used to MnO (1.032 V), FeO (1.61 V) and ZnO (1.252 V) and excludes TiO_2 (0.608 V for rutile and 0.625 V for anatase), SiO_2 (0.694 V) and Al_2O_3 (0.18 V); the voltages are given *versus* Li/Li^+.[26] In terms of capacity values and capacity retention, the best materials were found to be CoO and Co_3O_4 with reversible capacities of about 700 mA h g^{-1} and 900 mA h g^{-1}, respectively.[1] The drawback of cobalt is its high oxidation potential ranging from 2.2 to 2.4 V.[12,23] This means that the output cell voltage is going to be low, as shown by Badway *et al.* with a $Co_3O_4/LiCoO_2$ cell having an output voltage of only 2 V.[27] In addition, cobalt and nickel are expensive and toxic.[12] Iron is attractive because of:(i) its low cost, (ii) its environmental friendliness, and (iii) its experimental oxidation potential of 1.8 V, which is much lower than CoO, Co_3O_4 or NiO. Fe_3O_4 and Fe_2O_3 showed capacities of 745 mA h g^{-1} and 930 mA h g^{-1}, respectively.[20,21] Alternatives such as manganese oxides or zinc oxide are even more appealing when considering the low observed oxidation potential of these metal nanoparticles: 1.2 V and 1.5 V, respectively. These values will potentially increase the battery output voltage. In addition, their price is also much lower compared to nickel and cobalt. Zhong *et al.* reported reversible capacities for a MnO/carbon composite of 650 mA h g^{-1}.[18] As previously mentioned nanoparticles of zinc can further react with lithium and form a ZnLi alloy.[16,28] Unfortunately, due to the 163% volume expansion associated with the alloying process, a large irreversible capacity is observed for the first few cycles, and the reversible capacities ranging from 350 mA h g^{-1} to 500 mA h g^{-1} have been reported with a very low capacity retention upon cycling.[25,29]

Interestingly enough, combination of two TMOs, or a TMO and a post-transition metal oxide, in spinel-like structures, such as $ZnFe_2O_4$, have shown good capacity (615 mA h g^{-1}) on cycling.[30] Even though iron shows a higher oxidation potential than manganese and zinc, the AFe_2O_4 series (A = Co, Ni, and Zn) exhibit interesting capacity values for Li-ion battery applications: 700 mA h g^{-1} for $CoFe_2O_4$, 600 mA h g^{-1} for $NiFe_2O_4$, and 615 mA h g^{-1} for $ZnFe_2O_4$.[31] Another series, ACo_2O_4 (A = Zn or Cu), provided even higher capacity values: 800–900 mA h g^{-1} for $ZnCo_2O_4$[32,33] and 745 mA h g^{-1} for $CuCo_2O_4$ (after 50 cycles).[34] In addition, the ACo_2O_4 series show good capacity retention; however, as previously mentioned, the oxidation potential of Co is high and the voltage range to obtain the maximum capacity is large.[32] A similar series, manganites of TMs, have been briefly investigated by Pasero *et al.*[35] The off-stoichiometric $Co_{0.4}Mn_{2.6}O_4$ provided a stable capacity of about 400 mA h g^{-1}.[35] The most interesting manganite is $ZnMn_2O_4$, and due to the low price, abundance, and environmental friendliness of these two metals, it has been investigated once as anode material for Li-ion batteries. It was synthesized by a hydrothermal method, and it showed an adequate voltage range and capacity values of 626 mA h g^{-1} over 50 cycles.[36,37] Two other groups also reported the synthesis of $ZnMn_2O_4$: (i) Hem *et al. via* a slow coprecipitation method at 25 °C[38] and (ii) Selim *et al. via* a simple solid-state reaction.[39] However, none of these two groups showed applications for Li-ion batteries. In addition, there has been no report on the performance of the $CoMn_2O_4$ and $NiMn_2O_4$ as anode material for Li-ion batteries, to the best of our knowledge.

In this paper, we report the synthesis of three manganites, $CoMn_2O_4$, $NiMn_2O_4$, and $ZnMn_2O_4$, *via* a simple co-precipitation method. We also report their electrochemical and battery performance and compare them with that of their corresponding simple MOs. An extensive study was performed on the best performing manganite, $ZnMn_2O_4$, for which we investigated the effect of the following parameters: (i) the sintering temperature, (ii) the type of binder, (iii) the cycling temperature, and (iv) the type of electrolyte. Finally the performance of $ZnMn_2O_4$ was tested in a full cell battery using a $LiNi_{0.5}Mn_{1.5}O_4$ cathode (4.7 V).

Experimental

Materials

Manganese(II) acetate tetrahydrate (99+%), cobalt(II) acetate tetrahydrate (ACS, 98+%) or nickel(II) acetate tetrahydrate

(98%), oxalic acid (98%), *N*-methyl-2-pyrrolidone (NMP, anhydrous, 99.5%), poly3,4-ethylendioxythiophene-polystyrenesulfonate (PEDOT/PSS or Baytron, 1.5 wt% aqueous solution), lithium hexafluorophosphate ($LiPF_6$, 99.99%), ethylene carbonate (EC, anhydrous, 99%), dimethyl carbonate anhydrous (DMC, ≥99%), diethyl carbonate (DEC, anhydrous, ≥99%), and propylene carbonate (PC, anhydrous, 99.7%) were all purchased from Sigma-Aldrich. Zinc (II) acetate dihydrate (ACS, 98.0–101.0%) was purchased from Alfa Aesar. Cobalt (II) oxide was purchased from Aldrich and used as received. Carbon graphite E-KS4 and Super S carbon were obtained from Lonza G + T (Switzerland) and Timcal (Switzerland), respectively. Polyvinylidene fluoride (PVDF, Kynarflex2800) was purchased from Kynar and used as a 3 wt% solution in NMP. Sodium carboxymethyl cellulose (NaCMC, viscosity 42.0 mPa·s) was bought from Calbiochem and used as a 5 wt% solution dissolved in double distilled H_2O. Lithium carboxymethylcellulose (LiCMC) was made in house as reported in ref. 40. LiCMC was used as a 2.5 wt% solution dissolved in double distilled H_2O. Xanthan gum (XG) was obtained from Jungbunzlauer and used as a 1 wt% solution in double distilled H_2O. Finally, 30 μm thick microporous polypropylene separators #3501 were purchased from Celgard.

Synthesis

$ZnMn_2O_4$ was synthesized through a co-precipitation route using oxalic acid. Zinc (II) acetate and manganese (II) acetate were dissolved in deionized water (0.4 M) and added dropwise to an oxalic acid solution (0.4 M), heated at 75 °C, in a 1.5 : 1 oxalic acid : metal molar ratio. The precipitate was then filtered, dried and calcined at 400 °C, 600 °C, 800 °C, or 1000 °C. $CoMn_2O_4$ and $NiMn_2O_4$ powders were prepared using the same method using cobalt (II) acetate or nickel (II) acetate; their precipitates were calcined at 800 °C and 400 °C, respectively. NiO, ZnO and Mn_2O_3 were also prepared using the same method; NiO was calcined at 400 °C, and ZnO and Mn_2O_3 were calcined at 600 °C.

Characterization

Powder X-ray diffraction was carried out using a Bruker AXS D8 diffractometer with a Cu Kα source (or a Co Kα source when specified) with a divergence angle of 0.3°, a step size of 0.027°, and 1 s per step. The patterns were analyzed by the Rietveld refinement method[41] using the software TOPAS 4 from Bruker AXS.[42] The crystallite sizes were determined using the fundamental parameter approach method developed by Cheary *et al.*[43] The materials were further characterized by scanning electron microscopy (SEM) using a JEOL 840A and by transmission electron microscopy (TEM) using a Philips CM 20 microscope operating at 200 kV. The thermogravimetric analysis (TGA) was performed on the zinc-manganese oxalate precipitate using platinum pans in order to characterize the thermal decomposition of oxalates using a Hi-Res TGA 2950 TA instrument. The powder was heated at 10 °C min^{-1} up to 900 °C in air.

The electrochemical performance was studied using 2325-type coin cells assembled in an argon-filled dry box. The active material was mixed in a slurry containing 80 wt% of active material, 5 wt% of graphite E-KS4 (KG, Lonza G + T, Switzerland), 5 wt% Super S carbon (Timcal graphite and Carbon, Switzerland) and 10 wt% of binder. Five different binders were investigated: PVDF, NaCMC, LiCMC, XG, and Baytron. The slurry was cast onto a copper foil current collector that was cleaned using a 2.5% HCl solution in water. The cast was prepared using an automated doctor blade spreader and dried overnight in a convection oven at 85 °C and then in a vacuum oven for 18 h at 80 °C. Individual electrodes (Ø12.5 mm) were punched out, dried at 80 °C under vacuum overnight, pressed under a pressure of 0.5 metric ton, and were used as positive electrodes. A lithium disk (Ø 16.5 mm) was used as a negative electrode (counter electrode and reference electrode). 70 μL of a solution of 1 M $LiPF_6$ in EC : DMC (1 : 1 by vol.) was used as electrolyte and spread over a double layer of the polypropylene separators. The cells were galvanostatically cycled between 10 mV and 3 V at rates ranging from C/10 to 3C using an Arbin battery cycler. Cyclic voltammetry was carried using either a Biologic SP-150 or VMP3 potentiostat and swept at 0.1 mV s^{-1} between 10 mV and 3 V *versus* Li/Li^+.

Results and discussion

Thermogravimetric analysis

A TGA analysis has been performed during the decomposition process of zinc and manganese oxalates. Fig. 1 shows the thermal decomposition of this oxalate mixture in air. A first weight loss of 18.6 wt% was observed at 120 °C; it corresponds to the loss of the hydration water of the metal oxalates (two H_2O per metal oxalate).[44] The second and the third weight losses of 33.4 wt% and 5.8 wt%, respectively, correspond to the thermal decomposition of the oxalates. The third weight loss corresponds to the loss of a CO fragment. When considering both weight losses (step 2 and 3) of 39.2 wt%, it matches well the oxalates decomposition and the formation of $ZnMn_2O_4$. A total weight loss of 57.76 wt% was observed during the entire thermal decomposition.

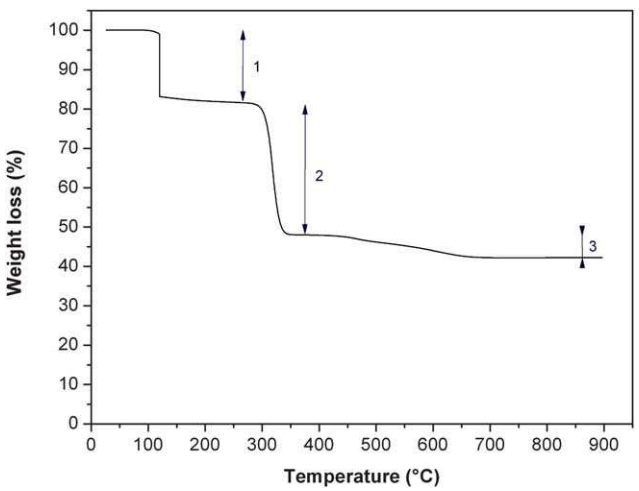

Fig. 1 TGA graph of the thermal decomposition of zinc and manganese oxalates in air.

X-Ray diffraction

XRD patterns of the three synthesized TM manganites, $CoMn_2O_4$, $NiMn_2O_4$ and $ZnMn_2O_4$, along with those of ZnO, Mn_2O_3, NiO and CoO were obtained at different sintering temperatures and are shown in Fig. 2 (in the ESI, S1† for NiO and CoO).

Fig. 2a shows the XRD patterns of $ZnMn_2O_4$ calcined at 400 °C, 600 °C, 800 °C, and 1000 °C. Indexing the patterns showed that a $ZnMn_2O_4$ $I4_1/amd$ tetragonal spinel structure was obtained for all sintering temperatures; the lattice parameters (*a* and *c*) have been determined by Rietveld refinement[41] and have been found to vary with the sintering temperature. As shown in Table 1, the *a* parameter decreased from 5.7294(9) Å at 400 °C to 5.7172(1) Å at 1000 °C, while the *c* parameter increased from 9.171(2) Å at 400 °C to 9.2497(1) Å at 1000 °C. These values correspond to an increase of the cell volume from 300.9 $Å^3$ at 400 °C to 302.4 $Å^3$ at 1000 °C. In the obtained spinel structure, Zn atoms occupy the 4*a* tetrahedral sites and Mn atoms occupy the 8*d* octahedral sites.[38] However, the cell parameter values showed that an important structural change occurred when the calcination temperature was increased from 400 °C to 800 °C: a decrease of the *a* parameter and an increase the *c* parameter (see Table 1). The Rietveld refinement showed that this is due to the deficiency of electron density on the 4*a* tetrahedral sites, either by a mixed occupancy of Zn and Mn atoms or by the presence of vacancies on the 4*a* sites (see Table 2). At 400 °C, a mixed occupancy of 73(8)% for Zn and 27(8)% for Mn or the presence of 7(7)% vacancies on the 4*a* site has been calculated by Rietveld refinement. In both cases, by increasing the sintering temperature, the calculated Zn occupancy of the 4*a* tetrahedral site increases up to 98–99% at 1000 °C. Even though at 400 °C only the $ZnMn_2O_4$ crystalline structure has been detected (by XRD), the decomposition of the oxalates is not totally completed, as shown by the TGA measurements, which explains the structural change that occurred from 400 °C to 600 °C and 800 °C. Over 600 °C only minor change has been observed and, as shown by TGA, over 700 °C no more weight loss has been observed, which matches well with the absence of a crystalline change between 800 °C and 1000 °C. Irani *et al.* conducted a study on the effect of the temperature on the cell parameters of $ZnMn_2O_4$ *via in situ* XRD measurements and pointed out a structural distortion due to the Mn^{3+} ions located in octahedral sites.[45] However in our case the X-ray patterns were measured at room temperature and the powder was slowly cooled down from its calcinations temperature to room temperature so no such distortion was observed.

As shown in Table 1, as expected, the crystallite sizes increased with the augmentation of the sintering temperature: from 11.4(2) nm at 400 °C to 324(14) at 1000 °C. In addition of being very fast, simple, and easy to scale up, the co-precipitation method presented here has the advantage of providing a spinel $ZnMn_2O_4$ structure without evidence of detectable crystalline impurities (by XRD) at a sintering temperature as low as 400 °C; for a solid-state synthesis, a sintering temperature of 800 °C is needed to obtain only the spinel $ZnMn_2O_4$ crystalline structure.[39]

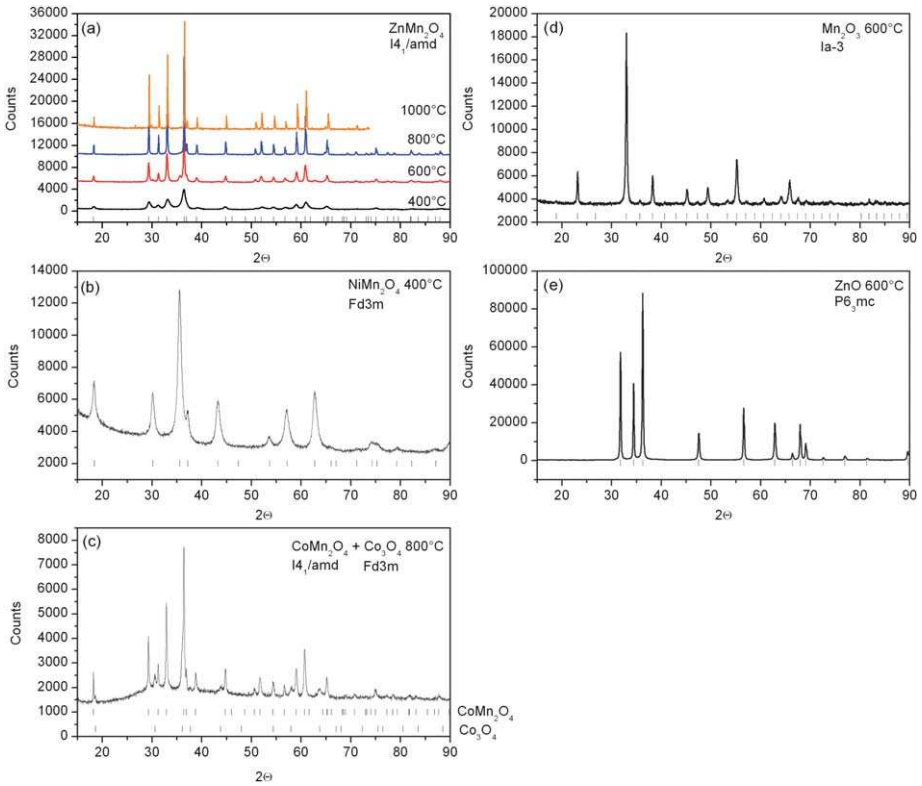

Fig. 2 Powder XRD patterns (Cu Kα) of (a) $ZnMn_2O_4$ sintered at 400 °C, 600 °C, 800 °C, 1000 °C (the 1000 °C was measured with a Co Kα X-ray source however 2Θ values are shown *versus* Cu Kα); (b) $NiMn_2O_4$ sintered at 400 °C; (c) $CoMn_2O_4$ sintered at 800 °C; (d) Mn_2O_3 sintered at 600 °C; and (e) ZnO sintered at 600 °C.

Table 1 XRD parameters of the prepared manganites

Manganite	Sintering temperature/°C	Space group	*a* parameter/Å	*c* parameter/Å	Cell volume/Å^3	Crystallite size/nm
$ZnMn_2O_4$	400	$I4_1/amd$	5.7294(9)	9.171(2)	300.9	11.4(2)
	600		5.7191(2)	9.2402(3)	302.2	33(1)
	800		5.7174(1)	9.2509(1)	302.5	130(3)
	1000		5.7172(1)	9.2497(1)	302.4	324(14)
$CoMn_2O_4$	800	$I4_1/amd$	5.7243(4)	9.2888(8)	304.4	65(27)
$NiMn_2O_4$	400	$Fd\bar{3}m$	8.3689(3)	—	586.2	11(1)

X-Ray diffractograms of $CoMn_2O_4$ and $NiMn_2O_4$ powders calcined at 800 °C and 400 °C, respectively, are shown in Fig. 2b and 2c. $NiMn_2O_4$ does not show a spinel structure but an inverse spinel structure; it exhibits a $Fd\bar{3}m$ cubic structure where, according to Bodak *et al.*, a mixed occupancy of the 4*b* tetrahedral sites and 8*c* octahedral sites occurs: 78.75% of Mn^{3+} on the 4*b* sites and 39.37% Ni^{2+} on the 8*c* sites.[46] Using the Rietveld refinement,[41] a cell parameter $a = 8.3689(3)$ Å and crystallite sizes of 11(1) nm were obtained. No crystalline impurity has been detected by XRD. As shown in Fig. 2c, $CoMn_2O_4$ exhibits the typical $I4_1/amd$ tetragonal spinel structure similar to $ZnMn_2O_4$ where, according to Hem *et al.*, Co^{2+} ions occupy 84% of the 4*a* tetrahedral sites and Mn^{3+} occupy 92% of the 8*d* octahedral sites.[47] Using the Rietveld refinement method[41] and the fundamental parameter approach method,[43] crystallite sizes of 65(27) nm and cell parameters of $a = 5.7243(4)$ Å and $c = 9.2888(8)$ Å were obtained, which correspond to a cell volume of 304.4 Å^3. In addition to $CoMn_2O_4$, a 17 wt% of Co_3O_4 has been observed as impurities in the powder. The larger cell volume, compared to $ZnMn_2O_4$, is most probably due to the mixed occupation of tetrahedral and octahedral sites. Only X-ray patterns of $NiMn_2O_4$ and $CoMn_2O_4$ sintered at 400 °C and 800 °C, respectively, have been presented since these powders provided the best capacity values when compared to other sintering temperatures.

Fig. 2d and e shows the X-ray patterns of the zinc oxide and manganese oxide powders sintered at 600 °C; the patterns confirm that ZnO hexagonal $P6_3mc$ structure and a Mn_2O_3 $Ia\bar{3}$ cubic structure were obtained. The Rietveld refinement provided cell parameters for ZnO of $a = 3.2510(7)$ Å and $c = 5.2090(1)$ Å. A cell parameter of $a = 9.412(5)$ Å was calculated for Mn_2O_3. Crystallite sizes of 66.9(5) nm and 49.4(8) nm were obtained for ZnO and Mn_2O_3, respectively. Only X-ray patterns of ZnO and Mn_2O_3 sintered at 600 °C are presented here since these powders have been used to compare the battery performance with $ZnMn_2O_4$ sintered at 600 °C. X-ray patterns of NiO sintered at 600 °C and commercial CoO are available in the ESI, S1†. No crystalline impurity has been detected by XRD in any of the above cases.

Table 2 Occupancy of the 4*a* tetrahedral site of $ZnMn_2O_4$ sintered at different temperatures

Sintering temperature/°C	Zn/Mn mixed occupancy		Zn/vacancies occupancy	
	Zn	Mn	Zn	Vacancies
400	0.73(8)	0.27(8)	0.930(7)	0.070(7)
600	0.87(5)	0.12(5)	0.959(4)	0.041(4)
800	1.00(3)	0.00(3)	0.970(3)	0.030(3)
1000	0.98(5)	0.02(5)	0.984(5)	0.016(5)

Scanning electron microscopy (SEM) and transmission electron microscopy (TEM)

The SEM micrographs of $ZnMn_2O_4$ powders sintered at 400 °C, 600 °C, 800 °C, and 1000 °C are shown in Fig. 3. The $ZnMn_2O_4$ powder sintered at 400 °C shows micrometric aggregates with sizes ranging from 1 to 5 μm. As expected, when the powder was sintered at 600 °C, larger aggregates were obtained with an average size of about 2 to 10 μm. At 800 °C, the morphology drastically changed and porous-cracked flakes of about 10 μm wide were obtained, whereas at 1000 °C the particles forming the porous-cracked flakes fused.

The TEM micrographs of $ZnMn_2O_4$ powders sintered at 400 °C, 600 °C and 800 °C, and close up SEM micrograph of $ZnMn_2O_4$ sintered at 1000 °C, are shown in Fig. 4. At 400 °C, particle sizes ranging from 5 to 10 nm are observed, at 600 °C particles of about 30–40 nm are obtained, at 800 °C particle sizes going from 75 to 150 nm are achieved, and at 1000 °C particles ranging from 500 nm to 1 μm are observed. The particle size increased with the augmentation of the sintering temperature, which is in agreement with the crystallite sizes obtained from the Rietveld refinement of the XRD patterns.

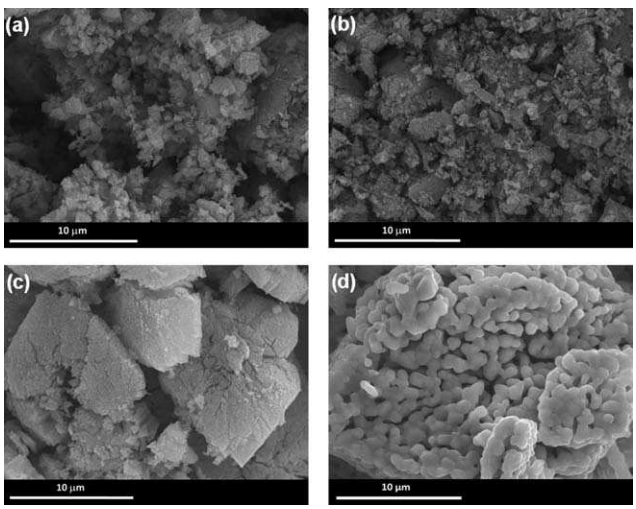

Fig. 3 SEM micrographs of $ZnMn_2O_4$ sintered at (a) 400 °C, (b) 600 °C, (c) 800 °C, and (d) 1000 °C.

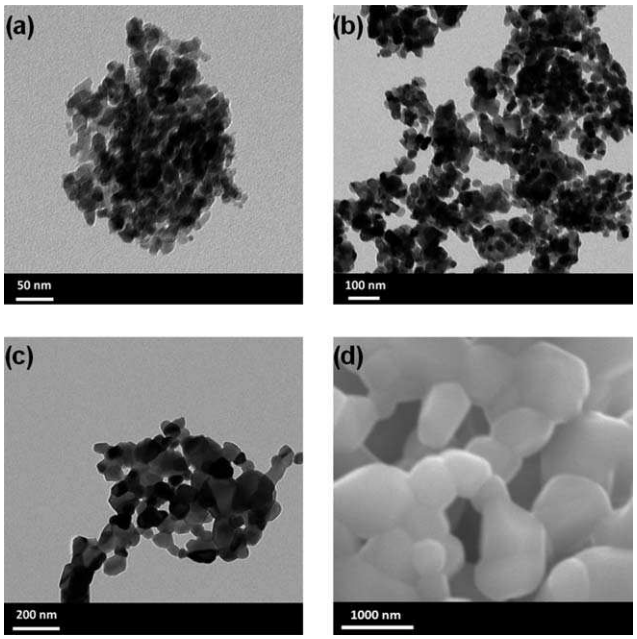

Fig. 4 TEM micrographs of $ZnMn_2O_4$ sintered at (a) 400 °C, (b) 600 °C, and (c) 800 °C; SEM micrograph of $ZnMn_2O_4$ sintered at (d) 1000 °C.

TEM micrographs of $NiMn_2O_4$ calcined at 400 °C and $CoMn_2O_4$ calcined at 800 °C are shown in Fig. 5. For $NiMn_2O_4$, 10 nm particles were obtained, which is in agreement with the crystallite size and the fact that low calcination temperatures usually provide smaller particles; whereas for $CoMn_2O_4$, calcined at 800 °C for 2 h, particles with 200–500 nm in size were obtained.

Cyclic voltammetry

Cyclic voltammetry measurements were performed in order to determine the experimental MO reduction potential (first cycle and subsequent cycles) and the oxidation potential of the metal nanoparticles. Fig. 6a and b shows the first and the second cycles of half-cells made using Mn_2O_3 and ZnO as active materials, respectively. The chosen sintering temperature was 600 °C for both oxides. These batteries were cycled at 0.1 mV s^{-1} between 10 mV and 3 V *versus* Li/Li^+. Both cyclic voltammograms show a different reduction peak position between the first and the second cycles. For Mn_2O_3, the first reduction process at 1 V corresponds to the reduction of Mn^{3+} to Mn^{2+}; this process occurs only during the first cycle. A second reduction process happens at a very low potential that corresponds to the reduction of Mn^{2+} to nanodomains of Mn^0 embedded in a Li_2O matrix. During the anodic sweep, the oxidation of Mn^0 to nanodomains of MnO occurs at 1.5 V, along with the decomposition of the Li_2O matrix. The anodic potential sweep is stopped at 3 V, which does not allow for the oxidation of Mn^{2+} to Mn^{3+}. As expected, there is a large difference between the oxidation and the reduction potentials due to the high overpotential characteristic of conversion reactions. The second cycle does not show any reduction of Mn^{3+} to Mn^{2+} but shows the reduction of Mn^{2+} to Mn^0 that happens at 0.2 V, which is explained by the fact that smaller particles show smaller overpotentials. Comparatively, the oxidation reaction does not change significantly during the first and the second oxidations. As shown in Fig. 6b, in the case of ZnO, the reduction process of the first cycle occurred between 0.25 and 0 V. This process corresponds to the reduction of Zn^{2+} to nanodomains of Zn^0 embedded in a Li_2O matrix, followed by the alloying reaction of Zn with Li to form ZnLi. During the anodic sweep, the first oxidation process between 0.25 and 0.75 V corresponds to the dealloying reaction to the ZnLi, as demonstrated by Wang *et al.*[28] The second process at about 1.5 V corresponds to the oxidation of Zn^0 to Zn^{2+} and the decomposition of the Li_2O matrix. During the second cathodic sweep, the reduction of the nanoparticles of ZnO occurred at a higher potential (between 1 V and 0.5 V) followed by the alloying reaction of Zn with Li. Both metals showed an oxidation reaction at about 1.5 V, which is pretty low for transition metals. For comparison, CVs showing the oxidation and reduction potentials associated with CoO and NiO electrodes are obtained and available in ESI, S2†. In these two cases, a higher reduction potential for the first cycle was also observed. In addition much higher oxidation potentials were obtained for Ni^0 and Co^0, which

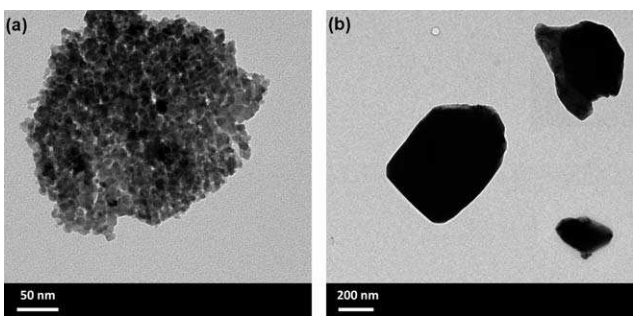

Fig. 5 TEM micrographs of (a) $NiMn_2O_4$ sintered at 400 °C and (b) $CoMn_2O_4$ sintered at 800 °C.

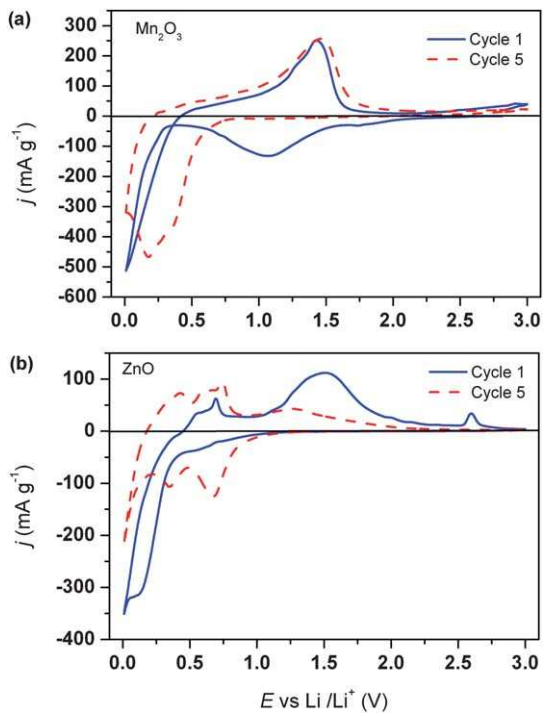

Fig. 6 Cyclic voltammograms of half-cells measured between 0.01 V and 3 V at 0.1 mV s^{-1} of (a) Mn_2O_3 and (b) ZnO, both sintered at 600 °C. Li metal was used as counter and reference electrode.

will decrease the output cell voltage of a full battery; oxidation potentials of about 2 V and 2.25 V were measured for Co^0 and Ni^0, respectively.

Fig. 7 shows the cyclic voltammogram of $ZnMn_2O_4$ sintered at 600 °C showing features similar to those of Mn_2O_3 and ZnO. During the first reduction, a peak can be observed at 1.1 V corresponding to the reduction of Mn^{3+} to Mn^{2+} followed by the reduction of Mn^{2+} and Zn^{2+} to nanodomains of Mn^0 and Zn^0, respectively, which occurs below 0.5 V. The first and subsequent oxidations peaks of Mn^0 and Zn^0 to Mn^{2+} and Zn^{2+} occur at 1.25 V and 1.6 V, respectively. The second and the subsequent reductions are shifted to 0.5 V. The cyclic voltammograms of $CoMn_2O_4$ and $NiMn_2O_4$ sintered at 800 °C and 400 °C, respectively, are shown in ESI, S3†.

Battery cycling

Cycling performance of ZnO and Mn_2O_3, *vs.* $ZnMn_2O_4$. Fig. 8 shows the discharge capacities at C/10 of half-cells made of ZnO, Mn_2O_3, or $ZnMn_2O_4$ active materials sintered at 600 °C; lithium metal was used as counter and reference electrode. Conventional binder, PVDF, cannot be used with this type of materials as it was shown that its elongation of up to 10% cannot accommodate volume changes during battery cycling and also the lack of strong interactions with the active materials compared to the more appropriate cellulose-based binders. In this work we have used the commercial NaCMC as a binder. Eqn (1) to (5) show the conversion reactions of Mn_2O_3, ZnO, and $ZnMn_2O_4$ with lithium. As shown by eqn (1) and (2), the theoretical first discharge capacity of Mn_2O_3 is 1019 mA h g^{-1}, and a maximum reversible capacity of 679 mA h $g^{-1}$of Mn_2O_3 is expected, due to the oxidation of Mn^0 to Mn^{2+} only. Experimentally, a first discharge capacity of 1117 mA h g^{-1} was obtained and a second discharge capacity of 605 mA h g^{-1} was measured, which agrees well with the theoretical values. However, the capacity rapidly decreased below 300 mA h g^{-1} after only 15 cycles. As shown by eqn (3), the reversible conversion reaction of ZnO to a ZnLi alloy can provide a theoretical capacity of 998 mA h g^{-1}. Unfortunately, experimentally ZnO did not show better capacity

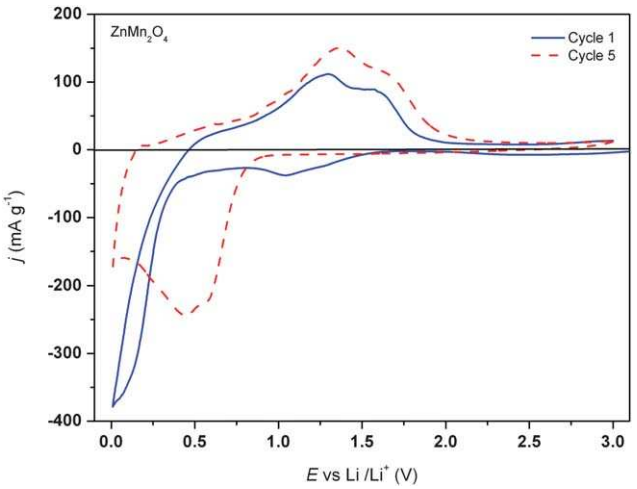

Fig. 7 Cyclic voltammograms of half-cells recorded between 0.01 V and 3 V at 0.1 mV s^{-1} of $ZnMn_2O_4$ sintered at 600 °C. Li metal was used as counter and reference electrode.

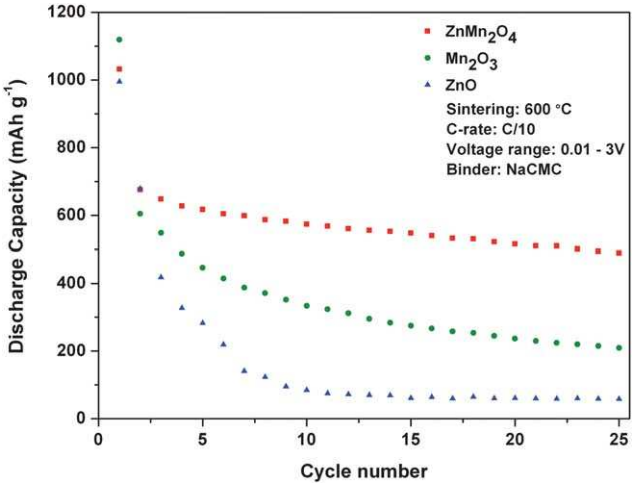

Fig. 8 Discharge capacities of ZnO, Mn_2O_3, and $ZnMn_2O_4$ electrodes prepared from powders sintered at 600 °C.

retention than Mn_2O_3, with a first discharge capacity of 995 mA h g^{-1}, which declined to 60 mA h g^{-1} after 12 cycles. It is important to point out that a volume change of 163% is associated with the formation of the alloy ZnLi, which explains the rapid fade of the capacity.[25] However, the manganite spinel $ZnMn_2O_4$ also sintered at 600 °C showed better performance compared to its simple MOs. The conversion reactions of $ZnMn_2O_4$ are shown by eqn (4) and (5). The first discharge corresponds to the reduction of Zn^{2+} and Mn^{3+} to nanodomains of Zn^0 (then ZnLi) and Mn^0 embedded in a matrix of Li_2O; this reaction is associated with a theoretical capacity of 1008 mA h g^{-1}. The reversible reaction shown by eqn (5) corresponds to the decomposition of the ZnLi alloy, followed by the oxidation of Zn^0 and Mn^0 to Zn^{2+} and Mn^{2+} along with the reduction of Li_2O. A reversible theoretical capacity of 784 mA h g^{-1} is associated with this reaction. An overlay of the charge/discharge profiles of ZnO, Mn_2O_3, and $ZnMn_2O_4$ is shown in ESI, S4†

$$Mn_2O_3 + 6Li^+ + 6e^- \rightarrow 2Mn + 3Li_2O$$
1019 mA h g^{-1}/4585 mA h mL^{-1} (first discharge) (1)

$$Mn + Li_2O \leftrightarrow MnO + 2Li^+ + 2e^-$$
679 mA h g^{-1}/3055 mA h mL^{-1} (reversible reaction) (2)

$$ZnO + 3Li^+ + 3e^- \leftrightarrow ZnLi + Li_2O$$
988 mA h g^{-1}/5619 mA h mL^{-1} (reversible reaction) (3)

$$ZnMn_2O_4 + 9Li^+ + 9e^- \rightarrow ZnLi + 2Mn + 4Li_2O$$
1008 mA h g^{-1}/5221 mA h mL^{-1} (first discharge) (4)

$$ZnLi + 2Mn + 3Li_2O \leftrightarrow ZnO + 2MnO + 7Li^+ + 7e^-$$
784 mA h g^{-1}/4061 mA h mL^{-1} (reversible reaction) (5)

As shown by Fig. 8, a first discharge capacity of 1030 mA h g^{-1} and a second discharge capacity of 675 mA h g^{-1} were obtained experimentally. An irreversible capacity of 340 mA h g^{-1} was measured between the first charge and the first discharge, which corresponds to three Li^+ per $ZnMn_2O_4$ formula; this corresponds to an extra Li^+ than the theoretical prediction. The enhanced performance of $ZnMn_2O_4$ could be explained by the fact that a homogeneous mixing of the Zn and Mn atoms at the atomic scale is obtained, which limits the effect of the volume change associated with the formation of the ZnLi alloy. However, after 25 cycles, a capacity of only 490 mA h g^{-1} (2450 mA h mL^{-1}) was retained, which is lower than previously reported by Xiao *et al.*, with 626 mA h g^{-1} (3130 mA h mL^{-1}) over 50 cycles.[36,37]

Effect of the sintering temperature of $ZnMn_2O_4$. In order to improve the reversible capacity of half-cells made of $ZnMn_2O_4$, the effect of the sintering temperature has been investigated. Fig. 9 shows the discharge capacities obtained at C/10 for half-cells made of $ZnMn_2O_4$ sintered at 400 °C, 600 °C, 800 °C, and 1000 °C with NaCMC as a binder. $ZnMn_2O_4$ sintered at 400 °C shows a rapid decay of the capacity; after 70 cycles a capacity of only 255 mA h g^{-1} (1275 mA h mL^{-1}) was obtained. As previously discussed, the same capacity fade was observed with the powder sintered at 600 °C, which showed a capacity of 337 mA h g^{-1} (1685 mA h mL^{-1}) after 70 cycles. However, when the powder was sintered at 800 °C, a very stable capacity was obtained over 70 cycles reaching 620 mA h g^{-1} (3100 mA h mL^{-1}), which is quite similar to the 626 mA h g^{-1} obtained by Xiao *et al.* after 50 cycles.[36,37] Sintering the powder at higher temperature (1000 °C) did not improve the performance of the half-cell; a capacity of only 260 mA h g^{-1} (1300 mA h mL^{-1}) was obtained after 70 cycles.

The sintering temperature affects the morphology and the size of the particles, as previously discussed in the XRD and TEM/SEM sections. The relation between the particle size and the performance of half-cells made of $ZnMn_2O_4$ is in agreement with what was reported by Poizot *et al.* for Cu_2O.[12] They showed that even though the oxide crystallites are broken during the first cycle and re-oxidized to much smaller ones, there is an advantage of starting with initially larger particles.[12] The TEM micrographs showed that the powder calcined at 800 °C had particle sizes ranging from 75 to 150 nm. However, as explained by Poizot *et al.*, if the particles are too big, a lower stable capacity is obtained. We verified this by cycling half-cells made of 200–300 nm $ZnMn_2O_4$ particles calcined at 800 °C for 16 h (see in ESI, S5†) and 500–1000 nm $ZnMn_2O_4$ particles calcined at 1000 °C for 2 h; in both cases, a stable capacity of 310 and 260 mA h g^{-1} were obtained, respectively, after 70 cycles.

In Fig. 10 the capacity values of $ZnMn_2O_4$ half-cells obtained at cycle 70 are plotted as a function of the particle size that has been estimated by TEM (or SEM for 1000 °C), and the crystallite size calculated from the XRD patterns. The particle and crystallite sizes increase with the augmentation of the calcinations temperature and the calcinations time: 400 °C for 2 h, 600 °C for 2 h, 800 °C for 2 h, 800 °C for 16 h, and 1000 °C for 2 h. According to Fig. 10, an optimum particle size of about 75–150 nm is needed in order to obtain the best performance for $ZnMn_2O_4$ prepared using the co-precipitation method presented here.

Effect of the metal (A) in AMn_2O_4 manganites: $ZnMn_2O_4$, $CoMn_2O_4$, and $NiMn_2O_4$. Although manganites $NiMn_2O_4$ and $CoMn_2O_4$ are expected to require a high voltage range in order to maximize the capacity, they have been synthesized for the sake of comparing the behavior of the various members of the AMn_2O_4 series and also because of the fact that they have not been previously studied. $CoMn_2O_4$ and $NiMn_2O_4$ were readily synthesized, as evidenced by the XRD measurements. The synthesis of $CuMn_2O_4$, however, was unsuccessful in our synthetic conditions. $CoMn_2O_4$ sintered at 800 °C and $NiMn_2O_4$ sintered at 400 °C showed the best cycling data of all the sintering temperatures; for this reason they were chosen for comparison with $ZnMn_2O_4$. $CoMn_2O_4$ has a theoretical first discharge capacity of 921 mA h g^{-1} and a reversible capacity of 691 mA h g^{-1}; whereas for $NiMn_2O_4$ they are 922 mA h g^{-1} and 692 mA h g^{-1}, respectively. The lower theoretical capacity values

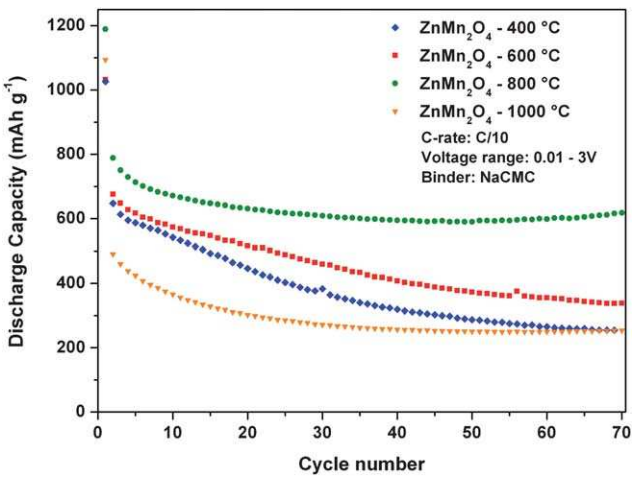

Fig. 9 Discharge capacities of $ZnMn_2O_4$ electrodes prepared from powders sintered at 400 °C, 600 °C, 800 °C, and 1000 °C.

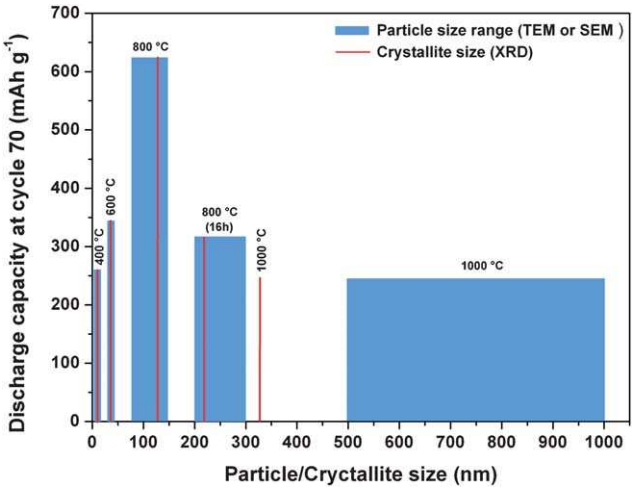

Fig. 10 Plot of the discharge capacity of $ZnMn_2O_4$ half-cells at cycle 70, as a function of the particle size (obtained by TEM or SEM) and the crystallite size (obtained by XRD) for different calcination temperatures: 400 °C (2 h), 600 °C (2 h), 800 °C (2 h), 800 °C (16 h), and 1000 °C (2 h).

compared to $ZnMn_2O_4$ are explained by the fact that neither Co nor Ni forms an alloy with Li. The equations of the conversion reactions of $CoMn_2O_4$ and $NiMn_2O_4$ are available in ESI, S6†.

Fig. 11 shows the charge and discharge profile of $ZnMn_2O_4$, $CoMn_2O_4$, and $NiMn_2O_4$ electrodes for the first two cycles only, while the cycling performance over several cycles is shown in Fig. 12. In the case of $ZnMn_2O_4$ and $CoMn_2O_4$, the main cathodic reactions with lithium occurred at about 0.4 V and are shown by a plateau. In the case of $ZnMn_2O_4$, the oxidation reactions are shown by a sloping voltage between 0.9 and 1.7 V and an irreversible capacity of 375 mA h g^{-1} was observed during the first cycle. The second cycle exhibits a sloping voltage between 0.8 V and 0.5 V. In the case of $CoMn_2O_4$, the oxidation process is shown by a sloping voltage that ranges from 0.3 to 2.1 V. In addition, a larger irreversible capacity of 470 mA h g^{-1} was observed (also observed *via* cyclic voltammetry, see ESI, S3†). Like $ZnMn_2O_4$, the $CoMn_2O_4$ potential profile of the second cycle varies from the first one. In addition, the subsequent reversible discharge capacities of $CoMn_2O_4$ are also lower than that of $ZnMn_2O_4$. As shown in Fig. 12, after 50 cycles, $CoMn_2O_4$ exhibits a capacity of 330 mA h g^{-1}. $NiMn_2O_4$ is different from the two previous manganites by the fact that (i) it does not have a spinel crystalline structure and (ii) it exhibits a different first charge/discharge profile. The first discharge showed a shoulder at about 0.9 V, which could correspond to the formation of an SEI layer that did not appear at this position for the previous spinels. A plateau then appeared at about 0.7 V, corresponding to the reduction of Ni^{2+} to Ni^0. During the charge, the oxidation process is shown by a sloping voltage that ranges from 0.3 to 2 V. An irreversible capacity of 210 mA h g^{-1} was observed for $NiMn_2O_4$. This value almost corresponds to the predicted irreversible capacity due to the oxidation of Mn^0 to Mn^{2+} and not Mn^{3+}, in other words, two lithium (230 mA h g^{-1}) per $NiMn_2O_4$ formula. In addition, the capacity retention between the second and the fourth discharges is very good, but unfortunately it drastically drops after 10 cycles, as seen in Fig. 12. After 20 cycles, the capacity was below 250 mA h g^{-1}. This dramatic capacity fade could be explained by the adverse reaction of Ni nanoparticles with the electrolyte which leads to a thick organic SEI that does not allow lithium ions to travel through. According to the CV (not shown), the Ni reduction and oxidation peaks are drastically reduced in intensity after the 10th cycle.

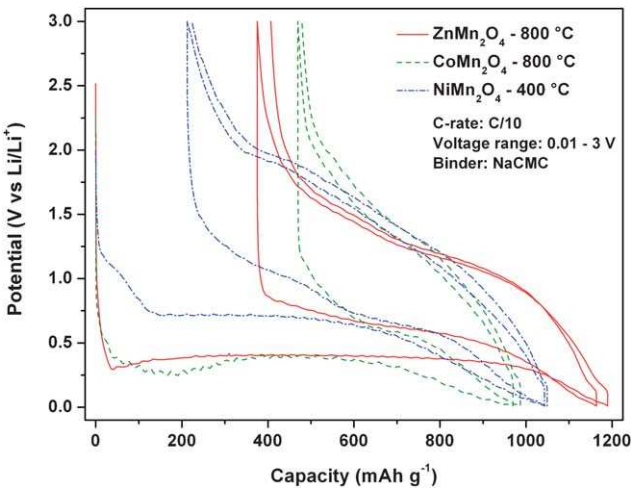

Fig. 11 Charge/discharge profile of $ZnMn_2O_4$, $CoMn_2O_4$, and $NiMn_2O_4$ electrodes prepared from powders sintered at 800 °C, 800 °C, and 400 °C, respectively; only the first two cycles are shown.

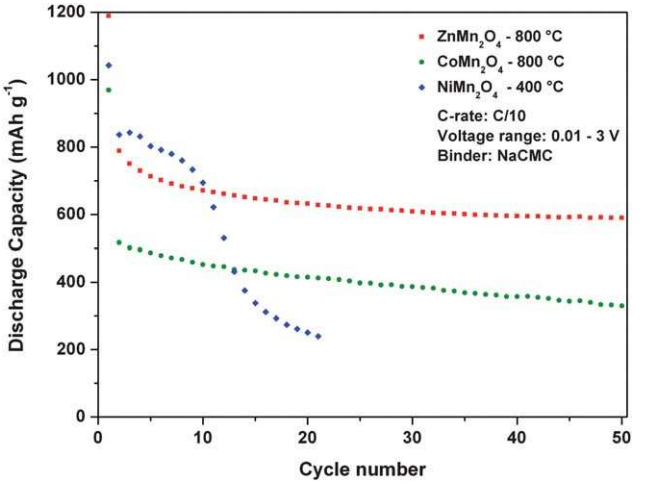

Fig. 12 Discharge capacities of $ZnMn_2O_4$, $CoMn_2O_4$, and $NiMn_2O_4$ electrodes prepared from powders sintered at 800 °C, 800 °C, and 400 °C, respectively.

Effect of the binder on the cycling performance of $ZnMn_2O_4$ sintered at 800 °C. Since the $ZnMn_2O_4$ powder sintered at 800 °C showed the best performance, only this material was used for the rest of the study. As previously mentioned, five different binders were investigated; the conventional one, PVDF dissolved in NMP, and four other water-soluble binders: NaCMC, LiCMC, XG, and Baytron. During the charge and discharge process, $ZnMn_2O_4$ undergoes volume changes mostly due to the formation of the ZnLi alloy. It is presumed that the binder used will affect the performance of the material. The electrochemical performance of $ZnMn_2O_4$ electrodes using these five binders is shown in Fig. 13. Since binders maintain the physical structure of the electrode, they are an important part of the electrode formulation. PVDF has been successfully used in commercial Li-ion batteries for decades since it exhibits excellent properties with materials that do not exhibit large volume change upon cycling. In addition, it is stable in a large electrochemical window at room temperature. However, it has several shortcomings. At elevated temperature, PVDF has been reported to react with anode materials to form fluorinated species *via* an exothermic reaction, which causes a risk for the onset of thermal runaway.[48–50] To avoid this risk, research has been focused on finding alternative non-fluorinated binders.[51–55] Another disadvantage of using PVDF is its price, which is about 20 US$ kg^{-1}.[56] As previously stated, PVDF is soluble in non-environmentally friendly solvents that are used to cast the electrodes, such as NMP. According to its material safety data sheet, NMP is known to be a mutagen, tumorigen and reproductive effector; its LD_{50} on rabbit skin is 8 mg kg^{-1}. Moreover, as mentioned by Lux *et al.* it is not easy to dispose PVDF at the end of the battery life.[56] Water soluble binders have already been investigated with some anode materials such as silicon and tin where more flexible and compatible binders are needed. Upon cycling, these active

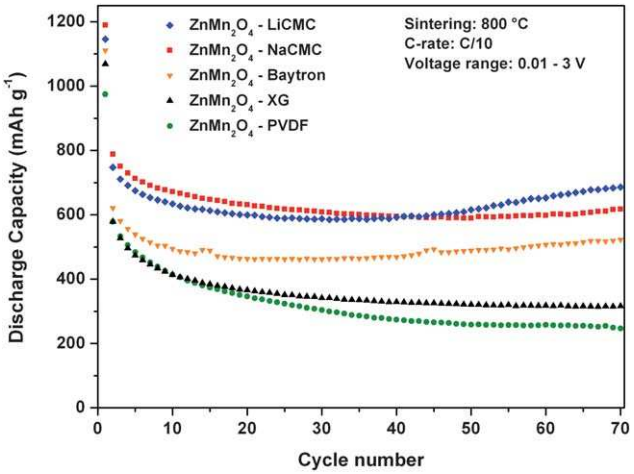

Fig. 13 Discharge capacities of $ZnMn_2O_4$ electrodes prepared from powders sintered at 800 °C and made using five different binders: PVDF, NaCMC, LiCMC, XG, and Baytron.

materials suffer from a large volume change between the charge and the discharge states (250–300%).[1] PVDF is not able to accommodate this large volume change. Binders such as styrene-butadiene rubber (SBR), NaCMC, and combinations of both were studied with silicon and provided great improvement of the capacity retention.[57–60] NaCMC has the advantage of being water soluble because of the carboxymethyl groups attached to cellulose. In addition, as stated by Lux *et al.*, the use of NaCMC as binder will make the recycling of Li-ion battery anodes much easier because the calcination of NaCMC at 700 °C yields Na_2CO_3, a naturally occurring mineral deposit.[56,61,62] In addition, its price is quite low, about 6 US$ kg^{-1}.[56] We already reported on the use of water soluble binders such as LiCMC, Baytron, NaCMC and XG with carbon MCMB.[40] They provided interesting performance. XG is more cost effective than PVDF, about 13 US$ kg^{-1}, whereas Baytron has the advantage of being electronically conductive (10 to 500 mS cm^{-1}) but more expensive.[63,64]

As shown in Fig. 13, the worst performance is obtained with PVDF as a binder. A first discharge slightly less than 1000 mA h g^{-1} was obtained, decreasing to 580 mA h g^{-1} on the second cycle and further to 300 mA h g^{-1} after 40 cycles but remained stable thereafter. Like NaCMC and LiCMC, XG is a cellulose-based binder; even though it provided very good performance with carbon MCMB,[40] it did not perform as expected with $ZnMn_2O_4$. After 30 cycles the capacity stabilized at 350 mA h g^{-1}, which represents about 45% of the theoretical reversible capacity of $ZnMn_2O_4$. Baytron, which is not particularly known for being an appropriate binder for materials that suffer from a large volume change upon cycling, provided better capacities than PVDF and XG. A first discharge capacity of 1110 mA h g^{-1} and then a stable discharge capacity of 510 mA h g^{-1} after 70 cycles were obtained, which corresponds to 65% of the reversible theoretical capacity. The two best binders were NaCMC and LiCMC; they both showed a higher first discharge capacity of 1190 mA h g^{-1} and 1145 mA h g^{-1}, respectively. After 70 cycles, 615 mA h g^{-1} or 78% of the reversible theoretical capacity was obtained when NaCMC was used as a binder. Interestingly enough, LiCMC provided higher capacity values of 690 mA h g^{-1} after 70 cycles, which represents 88% of the reversible theoretical capacity.

Using $ZnMn_2O_4$ sintered at 800 °C and LiCMC as a binder, we studied the rate capability of the half-cell made of this anode material. Prior to the study, the battery was cycled 40 times at C/10 in order to reach a stable capacity. It was then followed by increments consisting of five cycles at C/5, C/2, C, 2C, 3C, and then five additional cycles were performed at C/10. As shown by Fig. 14, the capacity after 40 cycles at C/10 is over 550 mA h g^{-1} and is almost unchanged at C/5. Capacities obtained for higher rates are 450 mA h g^{-1} for C/2, 340 mA h g^{-1} for C, 230 mA h g^{-1} for 2C, and 150 mA h g^{-1} for 3C rate. The capacity fully recovers to 600 mA h g^{-1} when the rate is switched to C/10, which makes this material very attractive for high rate cycling applications, such as plug-in hybrid electric vehicles.

Effect of the cycling temperature on the cycling performance of $ZnMn_2O_4$ sintered at 800 °C. Half-cells made using LiCMC as a binder with $ZnMn_2O_4$ particles sintered at 800 °C for 2 h have also been cycled at 60 °C. Fig. 15 shows a comparison of the cycling data at room temperature and 60 °C. Both batteries showed a similar first discharge and first irreversible capacity, 1145 mA h g^{-1} (5725 mA h mL^{-1}) and 400 mA h g^{-1}, respectively. Up to 10 cycles, both batteries showed similar performance, but upon cycling, the reversible capacity of the battery cycling at 60 °C increased more rapidly than the one cycled at room temperature. In addition, the difference between the charge and the discharge capacity is enhanced when the battery is cycled at 60 °C. This behavior is due to the growth of a polymeric organic layer at the surface of TMOs electrode. It happens at room temperature but is enhanced with the increase of the cycling temperature, as already observed by Poizot *et al.*[1] This polymeric organic layer is primarily made of decomposition products from the electrolyte solution (EC and DMC in this case). An interesting feature of this polymeric organic layer is that it can reversibly store lithium, which is the reason why the capacity of

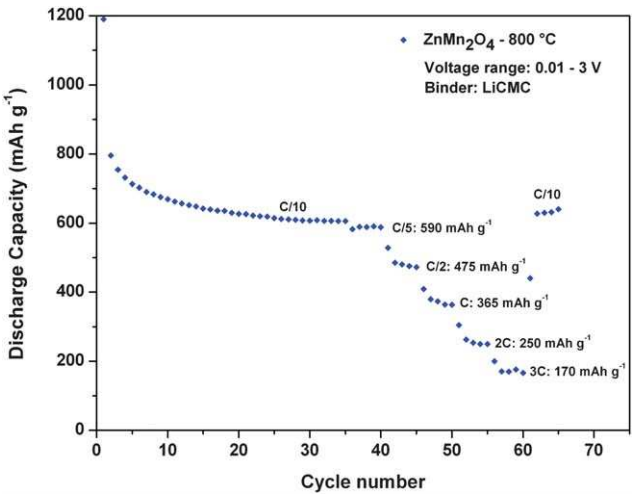

Fig. 14 Evaluation of the discharge rate capability of $ZnMn_2O_4$ electrodes prepared from powders sintered at 800 °C and made using LiCMC as binder.

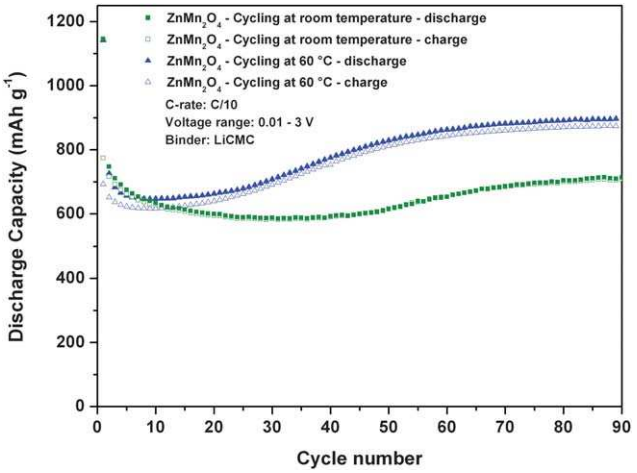

Fig. 15 Charge and discharge capacities of $ZnMn_2O_4$ electrodes prepared from powders sintered at 800 °C and made using LiCMC as binder. The half-cells were cycled at room temperature and at 60 °C.

the batteries increases with cycling.[1] The battery eventually reaches a maximum and the capacity starts fading.

Effect of the electrolyte on the cycling performance of $ZnMn_2O_4$ sintered at 800 °C. Fig. 16 shows the cycling performance of half-cells made using (i) $ZnMn_2O_4$ particles sintered at 800 °C for 2 h as an active material, (ii) LiCMC as a binder, and (iii) three different electrolytes: 1 M $LiPF_6$ with either the conventional EC : DMC (1 : 1 vol.), or EC : DEC (3 : 7 by vol.), or PC. The advantage of using a EC : DEC mixture is that it is usually more appropriate for high voltage cathode materials such as $LiMn_{1.5}Ni_{0.5}O_4$.[65] PC on the other hand has the advantage of providing a better ionic conductivity but is also known for not forming a stable SEI and for exfoliating graphite.[66] Therefore, PC is suitable and potentially beneficial for use in half-cell. For the 20 first cycles, all batteries exhibit almost the same reversible

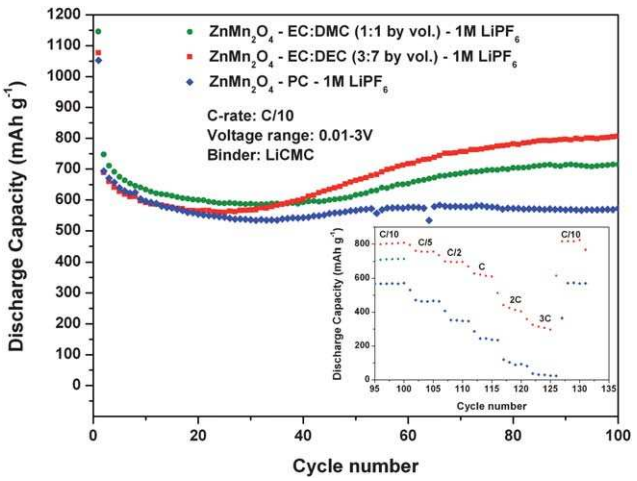

Fig. 16 Discharge capacities of $ZnMn_2O_4$ electrodes prepared from powders sintered at 800 °C and made using LiCMC as binder. The half-cells were cycled at room temperature using the same lithium salt, 1 M $LiPF_6$ in three different electrolytes: EC : DMC (1 : 1 by vol.), EC : DEC (3 : 7 by vol.), and PC.

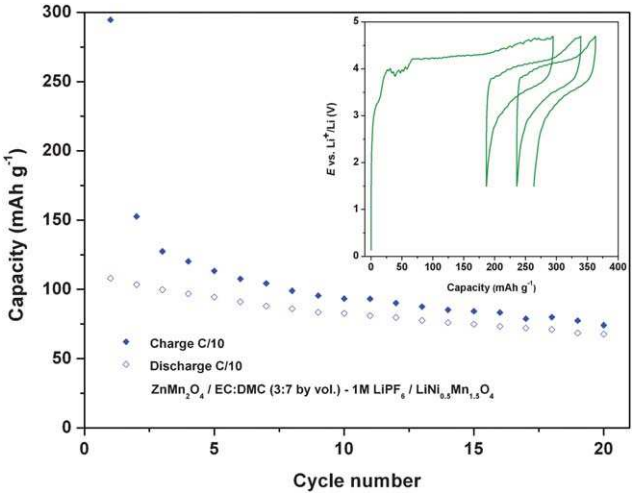

Fig. 17 Charge and discharge capacity of a $ZnMn_2O_4/LiMn_{1.5}Ni_{0.5}O_4$ full cell. Inset: voltage–capacity curve of $ZnMn_2O_4/LiMn_{1.5}Ni_{0.5}O_4$ full cell.

capacity; however, the capacity of the half-cell made using EC : DEC increases faster than the one made using EC : DMC. As previously explained, this capacity increase is due to the formation of an organic polymeric layer that reversibly stores lithium. After 100 cycles, a capacity of about 800 mA h g^{-1} (4000 mA h mL^{-1}) is obtained with EC : DEC, which represents 102% of the theoretical reversible capacity of $ZnMn_2O_4$. It is likely that the use of EC : DEC makes this layer grow faster than EC : DMC. On the other hand, when PC is used, the half-cell does not exhibit this capacity increase with cycling. This could be attributed to the fact that PC does not form this polymeric organic layer or that the layer formed with PC is inactive to lithium storage. PC provides a stable capacity of 675 mA h g^{-1} (3375 mA h g^{-1}), which corresponds to 86% of the theoretical reversible capacity of $ZnMn_2O_4$. A study of the electrode surfaces is currently under investigation.

A full Li-ion cell made of $ZnMn_2O_4/LiMn_{1.5}Ni_{0.5}O_4$. To the best of our knowledge, it is the first time that Li-ion batteries are assembled using $ZnMn_2O_4$ as an anode material, $LiMn_{1.5}Ni_{0.5}O_4$ as a cathode material,[65] and 1 M $LiPF_6$ in EC : DEC (3 : 7 by vol.) as the electrolyte. The battery performance is shown in Fig. 17. A Li-ion battery of this type is very challenging to assemble in terms of charge balance due to large discrepancies in the theoretical capacity of the two materials (5 : 1) and also due to the expected irreversible capacity during the first cycle. Therefore, in this case it was found that about 30% excess of cathode material was needed to obtain a well balanced $ZnMn_2O_4/LiMn_{1.5}Ni_{0.5}O_4$ cell. The cells were cycled between 1.5 V and 4.7 V at C/10 and the capacities were reported *versus* the limiting electrode (cathode). The initial capacity at a cycling rate of C/10 is 108 mA h g^{-1}, decreasing after 20 cycles to 68 mA h g^{-1}. During the first charge there is a plateau at 4.1 V; however, during the subsequent discharge and charge, the charge *vs.* voltage curve exhibits a sloping voltage between 3.5 V and 3 V and 3.5 and 4.1 V, respectively. Unfortunately, after 20 cycles, the battery exhibits a capacity of only 75 mA h g^{-1}.

Conclusions

In this paper, we presented a simple co-precipitation method to synthesize manganites of TMs, AMn_2O_4 (A = Co, Ni, Zn) and their performance in lithium batteries. $ZnMn_2O_4$ showed significant improvement in the capacity retention over the simple MOs ZnO and Mn_2O_3, while $CoMn_2O_4$ and $NiMn_2O_4$ gave either low or rapidly fading capacities. $ZnMn_2O_4$ sintered at 800 °C for 2 h has been found to be the most promising manganite. A study of $ZnMn_2O_4$ composites with different types of binders showed that LiCMC gave the best battery performance in terms of accommodating volume changes during cycling, by providing the highest discharge capacity (690 mA h g^{-1} or 3450 mA h mL^{-1}) and its retention (88%) over cycling. $ZnMn_2O_4$ also showed excellent rate capabilities with a recoverable capacity of 610 mA h g^{-1} at C/10 and 170 mA h g^{-1} at 3C. When cycled at 60 °C, a capacity increase was observed due to the growth of an organic polymeric layer on the anode; the effect of this layer was even more pronounced when EC : DEC (3 : 7 by vol.) was used as solvent whereas a lower but more stable capacity was obtained with PC. Finally, a $ZnMn_2O_4$/EC : DEC (3 : 7 by vol.)—1 M $LiPF_6$/$LiMn_{1.5}Ni_{0.5}O_4$ full cell was made and gave an initial capacity of 108 mA h g^{-1} with an average output voltage of 3.5 V.

Acknowledgements

The authors thank Natural Resources Canada's Program of Energy Research and Development for the financial support. The authors wish to thank Dr Dashan Wang for the TEM, Mr David Kingston for the SEM micrographs, and Dr Pamela Whitfield for her help and useful discussions regarding the XRD analyses. The authors are also very thankful to Maryam Nasirpour, Karina Yanez, Leo Cheng, and Dominique Duguay for their help with the experimental work. The authors also wish to thank Mr. P. Ahmaranian from Debro Chemical (Dorval, QC, Canada) who kindly provided the NaCMC and the XG binders.

References

1 G.-A. Nazri and G. Pistoia, *Lithium Batteries: Science and Technology*, Kluwer Academic Publisher, Boston, Dordrecht, New York, London, 2004.
2 T. D. Hatchard and J. R. Dahn, *J. Electrochem. Soc.*, 2004, **151**, A838–A842.
3 G. Derrien, J. Hassoun, S. Panero and B. Scrosati, *Adv. Mater.*, 2007, **19**, 2336–2340.
4 T. Brousse, O. Crosnier, J. Santos-Peña, I. Sandu, P. Fragnaud and D. M. Schleich, in *Materials Chemistry in Lithium Batteries*, ed. N. Kumagai and S. Komaba, Research Signpost, Kerala, 2002.
5 J. Hassoun, G. Derrien, S. Panero and B. Scrosati, *Adv. Mater.*, 2008, **20**, 3169–3175.
6 C. K. Chan, H. Peng, G. Liu, K. McIlwrath, X. F. Zhang, R. A. Huggins and Y. Cui, *Nat. Nanotechnol.*, 2008, **3**, 31–35.
7 J. Li, R. B. Lewis and J. R. Dahn, *Electrochem. Solid-State Lett.*, 2007, **10**, A17–A20.
8 U. Kasavajjula, C. Wang and A. J. Appleby, *J. Power Sources*, 2007, **163**, 1003–1039.
9 P. B. Balbuena and Y. Wang, *Lithium-Ion Batteries: Solid–Electrolyte Interphase*, Imperial College Press, London, 2004.
10 H. Inoue, in *International Meeting on Lithium Batteries, Biarritz (France)*, 2006.
11 P. G. Bruce, B. Dunn and J. W. Goodby, *Solid State Electrochemistry*, Cambridge University Press, Cambridge, UK, 2003.
12 P. Poizot, S. Laruelle, S. Grugeon, L. Dupont and J. M. Tarascon, *Nature*, 2000, **407**, 496–499.
13 B. Banerjee and S. Lahiry, *Phys. Status Solidi A*, 1983, **76**, 683–694.
14 V. I. Anisimov, M. A. Korotin and E. Z. Kurmaev, *J. Phys.: Condens. Matter*, 1990, **2**, 3973–3987.
15 H. Li, G. Richter and J. Maier, *Adv. Mater.*, 2003, **15**, 736–739.
16 A. N. Dey, *J. Electrochem. Soc.*, 1971, **118**, 1547–1549.
17 L. Xiao, Y. Yang, J. Yin, Q. Li and L. Zhang, *J. Power Sources*, 2009, **194**, 1089–1093.
18 K. Zhong, X. Xia, B. Zhang, H. Li, Z. Wang and L. Chen, *J. Power Sources*, 2010, **195**, 3300–3308.
19 Q. Fan and M. S. Whittingham, *Electrochem. Solid-State Lett.*, 2007, **10**, A48–A51.
20 W.-M. Zhang, X.-L. Wu, J.-S. Hu, Y.-G. Guo and L.-J. Wan, *Adv. Funct. Mater.*, 2008, **18**, 3941–3946.
21 L. Wang, H. W. Xu, P. C. Chen, D. W. Zhang, C. X. Ding and C. H. Chen, *J. Power Sources*, 2009, **193**, 846–850.
22 J. Kim, M. K. Chung, B. H. Ka, J. H. Ku, S. Park, J. Ryu and S. M. Oh, *J. Electrochem. Soc.*, 2010, **157**, A412–A417.
23 B. Varghese, M. V. Reddy, Z. Yanwu, C. S. Lit, T. C. Hoong, G. V. Subba Rao, B. V. R. Chowdari, A. T. S. Wee, C. T. Lim and C.-H. Sow, *Chem. Mater.*, 2008, **20**, 3360–3367.
24 S.-F. Zheng, J.-S. Hu, L.-S. Zhong, W.-G. Song, L.-J. Wan and Y.-G. Guo, *Chem. Mater.*, 2008, **20**, 3617–3622.
25 H. Wang, Q. Pan, Y. Cheng, J. Zhao and G. Yin, *Electrochim. Acta*, 2009, **54**, 2851–2855.
26 H. Li, P. Balaya and J. Maier, *J. Electrochem. Soc.*, 2004, **151**, A1878–A1885.
27 F. Badway, I. Plitz, S. Grugeon, S. Laruelle, M. Dolle, A. S. Gozdz and J. M. Tarascon, *Electrochem. Solid-State Lett.*, 2002, **5**, A115–A118.
28 J. Wang, P. King and R. A. Huggins, *Solid State Ionics*, 1986, **20**, 185–189.
29 C. Q. Zhang, J. P. Tu, Y. F. Yuan, X. H. Huang, X. T. Chen and F. Mao, *J. Electrochem. Soc.*, 2007, **154**, A65–A69.
30 Y. Sharma, N. Sharma, G. V. S. Rao and B. V. R. Chowdari, *Electrochim. Acta*, 2008, **53**, 2380–2385.
31 P. Lavela and J. L. Tirado, *J. Power Sources*, 2007, **172**, 379–387.
32 Y. Sharma, N. Sharma, G. V. Subba Rao and B. V. R. Chowdari, *Adv. Funct. Mater.*, 2007, **17**, 2855–2861.
33 Y. Qiu, S. Yang, H. Deng, L. Jin and W. Li, *J. Mater. Chem.*, 2010, **20**, 4439–4444.
34 Y. Sharma, N. Sharma, G. V. S. Rao and B. V. R. Chowdari, *J. Power Sources*, 2007, **173**, 495–501.
35 D. Pasero, N. Reeves and A. R. West, *J. Power Sources*, 2005, **141**, 156–158.
36 L. Xiao, Y. Yang, J. Yin, Q. Li and L. Zhang, *J. Power Sources*, 2009, **194**, 1089–1093.
37 Y. Yang, Y. Zhao, L. Xiao and L. Zhang, *Electrochem. Commun.*, 2008, **10**, 1117–1120.
38 J. D. Hem, C. E. Roberson and C. J. Lind, *Geochim. Cosmochim. Acta*, 1987, **51**, 1539–1547.
39 M. M. Selim, N. M. Deraz, O. I. Elshafey and A. A. El-Asmy, *J. Alloys Compd.*, 2010, **506**, 541–547.
40 F. M. Courtel, S. Niketic, D. Duguay, Y. Abu-Lebdeh and I. J. Davidson, *J. Power Sources*, 2010, **196**, 2128–2134.
41 H. Rietveld, *Acta Crystallogr.*, 1967, **22**, 151–152.
42 *BrukerAXS*, Karlsruhe, Germany, 2008.
43 R. W. Cheary and A. Coelho, *J. Appl. Crystallogr.*, 1992, **25**, 109–121.
44 A. Packter, *Krist. Tech.*, 1976, **11**, 1131–1138.
45 K. S. Irani, A. P. B. Sinha and A. B. Biswas, *J. Phys. Chem. Solids*, 1962, **23**, 711–727.
46 O. Bodak, L. Akselrud, P. Demchenko, B. Kotur, O. Mrooz, I. Hadzaman, O. Shpotyuk, F. Aldinger, H. Seifert, S. Volkov and V. Pekhnyo, *J. Alloys Compd.*, 2002, **347**, 14–23.
47 J. D. Hem and C. J. Lind, *Geochim. Cosmochim. Acta*, 1991, **55**, 2435–2451.
48 A. Du Pasquier, F. Disma, T. Bowmer, A. S. Gozdz, G. Amatucci and J. M. Tarascon, *J. Electrochem. Soc.*, 1998, **145**, 472–477.
49 H. Maleki, G. Deng, A. Anani and J. Howard, *J. Electrochem. Soc.*, 1999, **146**, 3224–3229.
50 H. Maleki, G. Deng, I. Kerzhner-Haller, A. Anani and J. N. Howard, *J. Electrochem. Soc.*, 2000, **147**, 4470–4475.
51 M. Gaberscek, M. Bele, J. Drofenik, R. Dominko and S. Pejovnik, *Electrochem. Solid-State Lett.*, 2000, **3**, 171–173.
52 G. Oskam, P. C. Searson and T. R. Jow, *Electrochem. Solid-State Lett.*, 1999, **2**, 610–612.

53 N. Ohta, T. Sogabe and K. Kuroda, *Carbon*, 2001, **39**, 1434–1436.
54 S. S. Zhang and T. R. Jow, *J. Power Sources*, 2002, **109**, 422–426.
55 M. W. Verbrugge and B. J. Koch, *J. Electrochem. Soc.*, 2003, **150**, A374–A384.
56 S. F. Lux, F. Schappacher, A. Balducci, S. Passerini and M. Winter, *J. Electrochem. Soc.*, 2010, **157**, A320–A325.
57 H. Buqa, M. Holzapfel, F. Krumeich, C. Veit and P. Novák, *J. Power Sources*, 2006, **161**, 617–622.
58 S. D. Beattie, D. Larcher, M. Morcrette, B. Simon and J. M. Tarascon, *J. Electrochem. Soc.*, 2008, **155**, A158–A163.
59 N. S. Hochgatterer, M. R. Schweiger, S. Koller, P. R. Raimann, T. Wohrle, C. Wurm and M. Winter, *Electrochem. Solid-State Lett.*, 2008, **11**, A76–A80.
60 W.-R. Liu, M.-H. Yang, H.-C. Wu, S. M. Chiao and N.-L. Wu, *Electrochem. Solid-State Lett.*, 2005, **8**, A100–A103.
61 G. D. O. Machado, A. M. Regiani and A. Pawlicka, *Polimery*, 2003, **48**, 273–279.
62 J. Kaloustian, A. M. Pauli and J. Pastor, *J. Therm. Anal. Calorim.*, 1997, **48**, 791–804.
63 H. C. Starck, http://nanomechanics.pratt.duke.edu/MSDS/3%204_Polyethylenedioxythiopenepolystyrenesulfonate.pdf, Number PD-6002, Issue 2–05.09, 2006.
64 http://www.sigmaaldrich.com.
65 H. Duncan, Y. Abu-Lebdeh and I. J. Davidson, *J. Electrochem. Soc.*, 2010, **157**, A528–A535.
66 K. Xu, *Chem. Rev.*, 2004, **104**, 4303–4418.